



# Surrogate-based robust design optimization by using Chebyshev-transformed orthogonal grid

Shizhao Jing<sup>1</sup> · Zebin Zhang<sup>1</sup> · Xianzong Meng<sup>1</sup>

Received: 21 March 2024 / Revised: 5 June 2024 / Accepted: 20 June 2024 / Published online: 16 July 2024  
© The Author(s), under exclusive licence to Springer-Verlag GmbH Germany, part of Springer Nature 2024

## Abstract

Surrogate-based aerodynamic robust design optimization uses a surrogate model to calculate the robustness indices, which strongly relies on the overall accuracy of the model, as well as the efficient exploration of the design space. For most surrogate modeling approaches, significant inaccuracies are often observed at the outlier region of the design space, where very few samples are spotted. A novel method using Chebyshev transformation is applied to re-allocate the orthogonal Latin hypercube sample set to alleviate the corner errors and eventually improve the overall accuracy. An inner Kriging model is developed using the sampling method, and robustness indices are calculated based on the subspaces adjacent to the sampling points. Subsequently, an outer robust model is constructed with the robustness indices as the target. Ultimately, a combination of the inner and outer models is utilized with the genetic algorithm to accomplish multi-objective robust optimization. Theoretical tests are undertaken for classic test functions, showing the advantage of the proposed approach. Based on this method, aerodynamic robust design optimizations are carried out on the RAE 2822 airfoil, for which the lift coefficient and drag coefficient are optimized for a given range of geometrical parameters. An increase of 1.94% lift coefficient and a reduction of 2.53% drag coefficient are achieved compared to the baseline design without sacrificing the robust performances.

**Keywords** Robust design optimization · Surrogate modeling · Sampling strategy · Chebyshev polynomial · Orthogonal grid

## 1 Introduction

Aerodynamic performance in transonic conditions involves various nonlinear physics, such as shock waves and separated flow (Zhao et al. 2019). Subtle fluctuations of operating conditions and/or geometrical distortion can have an amplified effect on the loading and eventually on the aerodynamic performances. To address this issue, robust aerodynamic design optimization is utilized to anticipate performance variations under various uncertainties. The variations in aerodynamic performance stem from uncertainties in the design variables and design/operating parameters. Global

robust optimization aims to identify a design that achieves a target response with minimal variation. This paper focuses on the uncertainty of design variables. However, the methodology in its mathematical formulation, can be applied to both types of uncertainties. Uncertainty analysis methods can be categorized as sampling, perturbation, and surrogate-based methods, among others, based on different stochastic simulation processes (Tang and Zhou 2015; Wu et al. 2018; Beyer and Sendhoff 2007). Among these techniques, the surrogate-based robust design optimization has become increasingly popular in aerodynamic shape design (Jiang et al. 2018; Hanazaki and Yamazaki 2024). Tao and Sun have developed a multi-fidelity surrogate-based optimization framework, which was used to optimize the robustness of transonic airfoils and wings (Tao and Sun 2019). Lee and Kwon (2006) compared the results of deterministic optimization with robust optimization and found that the latter achieved better robust performance. Jaeger et al. (2013) discovered that optimizing the wing with a smaller aspect ratio leads to more reliable and robust performance.

The advantages of surrogate-based robust design optimization lie in its overall representation of the design space,

---

Communicated by Zhen Hu.

✉ Zebin Zhang  
zebin.zhang@zzu.edu.cn

<sup>1</sup> School of Mechanical and Power Engineering, Zhengzhou University, Kexue Avenue, Zhengzhou 450001, Henan, China

involving an inner modeling process and an outer robust optimization process. These processes can be either iterative or independently successive. The former approach does not establish a determinant robust model. Instead, robustness indices are calculated and integrated into the optimization process using various stochastic simulation methods (Fang et al. 2021). When applying uncertainty quantification to models, varying uncertainties and model-related errors can significantly impact the robust solutions. In these cases, the focus is often on finding a better solution, rather than the best solution. Thus, this approach may not be ideal for black-box problems with a large number of computations, particularly those with high dimensions. Additionally, it is not well suited for systematic modeling of a given system.

The second method treats the two processes as a single loop. The surrogate and robust models are built and refined together until they reach maximum accuracy (Ribaud et al. 2020). The model is updated only if the robust solution is not satisfactory. This approach is a multi-objective optimization with robustness indices objectives, which is more widely used in engineering practices (Jones and Martins 2021; Pang et al. 2023). To calculate robustness, there are various methods available, such as Monte–Carlo simulation and polynomial chaos expansion (Zhao 2015). However, accurate modeling of the function of interest is essential for this approach to be effective.

To improve the accuracy of the modeling of design space, the two most critical characteristics considered are orthogonality and uniformity (Zhang et al. 2019; Song et al. 2018). Various sampling methods have been proposed to achieve this. For the measure of space infill, Fang and Wang proposed the  $L_\infty$  uniformity (Fang 1994), which is measured by the discrepancy. Latin hypercube sampling (LHS) is a multidimensional, stratified sampling method that can generate a variable number of samples. The LHS design ensures that only one sample represents each level in each dimension (Giunta et al. 2003). To address the issue of insufficient stability in LHS, Park (Leary et al. 2003) proposed an Optimal Latin Hypercube (OLH) sampling method to effectively improve the situation of poor distribution caused by the randomness of LHS. Nearly Orthogonal Latin Hypercube (NOLH) sampling takes into account four different criteria and dramatically improves the space-filling properties of the resultant LHS (Cioppa and Lucas 2007). Smolyak grids (S-G) or sparse grids are designed to efficiently approximate and integrate functions on multidimensional hypercubes (Ullrich 2008; Plaskota and Wasilkowski 2004).

However, a common challenge arises when calculating the robustness indices using the above sampling methods, particularly in the “extrapolating” region of the design space. The approximation often becomes less accurate, similar to the “Runge effect” observed when Lagrange interpolation uses isometric samples. This can directly impact the

calculation of the robustness indices and, in turn, the robust design results. Therefore, this study attempts to improve the overall accuracy of the surrogate model by rearranging the samples by Chebyshev transformation. The rearrangement will increase the number of samples in the outlier region, thus reducing the corner error of design space. Additionally, a robustness indices calculation method based on random sampling of neighborhood subspace is proposed to optimize the response and robustness simultaneously.

The structure of this paper is as follows: Sect. 2 introduces a novel sampling technique known as Chebyshev-transformed orthogonal grid sampling. In Sect. 3, we detail the process of calculating robustness indices using this approach and provide a robust design optimization process. The superiority of the proposed approach is testified by several test functions (Sect. 4), and it is applied to the robust aerodynamic optimization of RAE 2822 transonic airfoil (Sect. 5). Conclusions of this study and some perspectives are drawn in Sect. 6.

## 2 Chebyshev-transformed orthogonal grid

### 2.1 Runge effect and corner error

The Runge effect arises when constructing high-order polynomial interpolation using uniform nodes for certain functions. Significant errors are often observed at the edge of the interpolation interval, deteriorating the accuracy of high-order polynomial prediction. Many surrogates and kernel-based interpolants suffer the similar error (Zhang et al. 2014), as a result, different acquisition functions and sequential design approaches tend to allocate sampling points on the corners/borders of the design space (Wang et al. 2024; Iuliano 2019). Approaches that are capable of reducing the Runge effect are believed to be effective in reducing the above-mentioned corner errors.

The Runge effect reflects the following inequality:

$$\|f(x) - p_n^*(x)\|_\infty > \min_{p_n \in H_n} \|f(x) - p_n(x)\|_\infty, \quad (1)$$

where  $f(x)$  is the true function of interest,  $p_n^*(x)$  is the polynomial approximation and  $H_n$  is the set of all polynomials of an order less than  $n$ .

When creating complex surrogate models using traditional sampling methods, similar issues to the Runge effect may arise. This results in a large error at the edges of the design space, which reduces the overall accuracy of the model. This error, known as the “corner error,” may be less important in traditional optimization designs, but it becomes significant when robustness is introduced. Traditional optimization designs prioritize local accuracy near the optimal solution to improve optimization precision. Nevertheless,

it has been shown that even functions that are unimodal or monotonic may contain multiple local robust optimal solutions (Lee and Park 2006), resulting in a complex robust design problem. In these instances, any corner error can greatly impact the calculation of the robustness indices.

### 2.2 Chebyshev-transformed OLH sampling

The Runge effect can be addressed by utilizing Chebyshev polynomials. Potential theory suggests that a series of Chebyshev polynomials is a highly effective method for representing a smooth non-periodic function (Driscoll et al. 2014; Trefethen 2013). To optimize and reduce computational complexity, various methods of polynomial interpolation in Chebyshev points and expansion in Chebyshev polynomials have been proposed. Chebyshev polynomials are also frequently utilized as a surrogate model, particularly in the realm of uncertainty quantification (Wu et al. 2015; Fu et al. 2022). In conclusion, the use of Chebyshev polynomials is expected to achieve the following objectives:

$$\|f(x) - p_n^*(x)\|_\infty = \min_{p_n \in H_n} \|f(x) - p_n(x)\|_\infty. \tag{2}$$

Inspired by the solution of the Runge effect, Chebyshev polynomials are employed to address the corner error issue in this study. Instead of direct utilization for surrogate modeling, our approach focuses on leveraging Chebyshev polynomials to generate non-uniform sample sets (Zhang et al. 2024). The extrema of these polynomials, known as Chebyshev points of the second kind, are determined by projecting equiangular grids onto a unit circle, which can be mathematically expressed using the cosine rule:

$$x_i = \cos \frac{i\pi}{n_{ch}}, i = 0, 1, \dots, n_{ch}. \tag{3}$$

Figure 1 presents the process of creating Chebyshev extrema, where the samples are strategically placed at the ends of the interval to minimize corner error. Additionally, if there is a uniform or quasi-uniform sample set in an  $n$ -dimensional

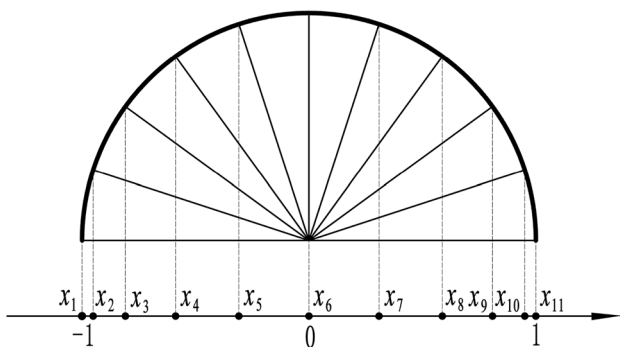


Fig. 1 The extrema of Chebyshev polynomials

space represented by an evenly distributed pattern on a hypersphere, the cosine rule can be employed to extend the extrema of the Chebyshev polynomials to a design space with dimensions.

The Chebyshev transformation process in a high-dimensional design space involves several important steps. First, it is crucial to obtain a set of initial samples. One reliable method for generating these points is through OLH sampling, which provides excellent uniformity and orthogonality and can generate any desired number of samples. When using this method, it is recommended to choose a design space range of  $[-1, 1]^n$  and determine the number of samples based on specific requirements. Once the OLH samples have been generated, the next step is to perform the Chebyshev transformation. For multi-dimensional problems, it is advisable to transform the coordinates of each dimension separately using the appropriate conversion formula:

$$x_{tr} = \cos \frac{(1 - x_{ini})\pi}{2}, \tag{4}$$

where  $x_{ini}$  is the initial coordinate of samples and  $x_{tr}$  is the transformed coordinate.

Then, a Chebyshev-transformed OLH sampling, referred to as Cheb-OLH sampling in this study, is generated. It is worth noting that  $x_{tr}$  ranges from  $-1$  to  $1$ . Therefore, it is necessary to adjust the design space based on the specific circumstances.

Figure 2 shows the comparison of the OLH sampling (Fig. 2a) and the Cheb-OLH sampling (Fig. 2b) in two dimensions. While the original OLH sampling is uniform, the points undergo a shift that aligns their projection onto each dimension with the one-dimensional Chebyshev extrema distribution. This transformation is intended to mitigate the adverse effects of the corner effect, which can compromise the accuracy of modeling.

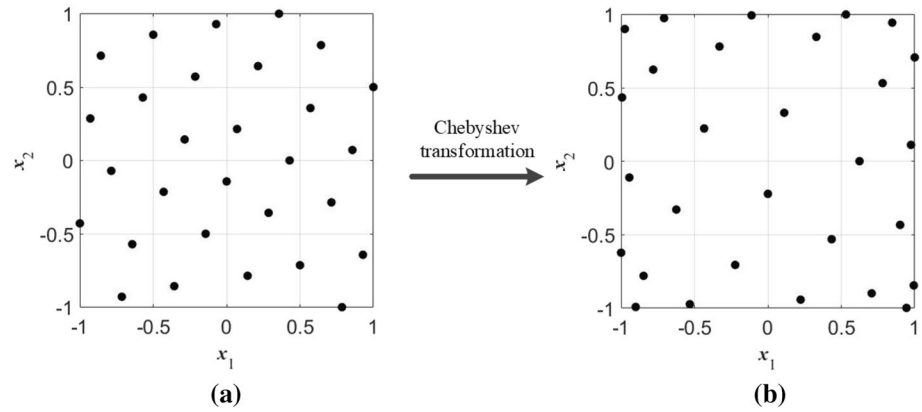
### 3 Surrogate-based robust design optimization

The Gaussian process in the category of Kriging models utilizes Gaussian distribution to stochastically model an unknown process. It comprises a regression function and a random variable that adheres to preset statistical rules. The approaches are supposed to have better nonlinear approximation and are able to provide theoretical error prediction as well as its distribution (Dong and Lu 2022), which are frequently employed to tackle black-box problems where the underlying mechanisms are unclear. The Kriging model is represented as follow:

$$\hat{y}(x) = \mathbf{F}^T(x)\beta + z(x), \tag{5}$$

where  $\hat{y}(x)$  is the function estimation of the unknown point,  $\beta$  is the regression coefficient,  $\mathbf{F}^T(x)$  is a polynomial in  $x$ ,

**Fig. 2** Comparison of two sampling methods. **a** OLH. **b** Cheb-OLH



used to model the period of the stochastic process, and  $z(x)$  is a random term.

The fluctuations in the response can be attributed to the uncertainties in the design variables. The primary objective of global robust optimization is to attain a design that yields the desired response with minimal variation. In this particular investigation, the Kriging model is employed to establish a precise and comprehensive mapping correlation between the design variables and response, as well as to compute the robustness indices. Additionally, the standard deviation is utilized to measure the robustness, which can be computed through the formula below:

$$\sigma_f = \sqrt{\frac{1}{m_{SS} - 1} \sum_{i=1}^{m_{SS}} (f_i - \mu_f)^2}, \tag{6}$$

where  $m_{SS}$  is the number of samples used in the stochastic simulation process;  $f_i$  is the response at the  $i$ th random sample; and  $\mu_f$  is the mean of the response values of all random samples. The standard deviation  $\sigma_f$  ranges from 0 to positive infinity by definition. However, in the context of purely mathematical modeling and prediction, which does not take the positive definition into account, hence there may be instances where the prediction result turns out to be negative, contrary to  $\sigma \geq 0$ . To address this, the natural log of the standard deviation  $\ln\sigma$  is employed as the robustness indices. It is important to emphasize that the standard deviation reflects the fluctuation of the response value and a lower standard deviation indicates higher robustness.

In this study, the Cheb-OLH sampling method is supposed to reduce corner error and improve the global accuracy of the Kriging model. Then, this model was utilized to conduct stochastic sampling in the subspace of samples, resulting in obtaining the standard deviations of the responses within the range. Additionally, the normal stochastic sampling was chosen to calculate the robustness indices, taking into account that the uncertainty of design variables in engineering is typically distributed. Once the responses

and robustness indices of all locations in the design space are calculated, the global robust optimization problem can be defined as

$$\text{Minimize } f(x), \ln\sigma_f.$$

An algorithm for global robust optimization is proposed using Cheb-OLH sampling and Kriging model. The steps of the proposed algorithm are as follows (Fig. 3):

**Step 1:** *Cheb-OLH sampling and construction of the inner Kriging model*

The set of samples, denoted as  $S$ , is obtained by the Cheb-OLH sampling method described in Sect. 2. Then, the responses  $Y$  at each sample can be obtained through experimentation or simulation. Finally, the Kriging model is established based on  $S$  and  $Y$ . The higher the accuracy of the model, the lower the error of the robustness indices, resulting in greater precision during optimization.

**Step 2:** *Calculations of robustness indices using normal stochastic sampling*

In this step, the inner Kriging model is utilized to determine the standard deviation for the outer robust model. To obtain additional information in the design space, uniform sampling is employed, gathering  $S_{RO}$  from the design space. Normal stochastic sampling was adopted in the subspace of each sample in  $S_{RO}$ . The size of the subspace is established at 5% of the design space and the number of stochastic samples was initially set at  $m_{SS}$ . Finally, responses of  $m_{SS}$  samples is predicted and  $\ln\sigma$  is calculated. This process is not a computational burden since the surrogate approximate model is represented by mathematical expressions.

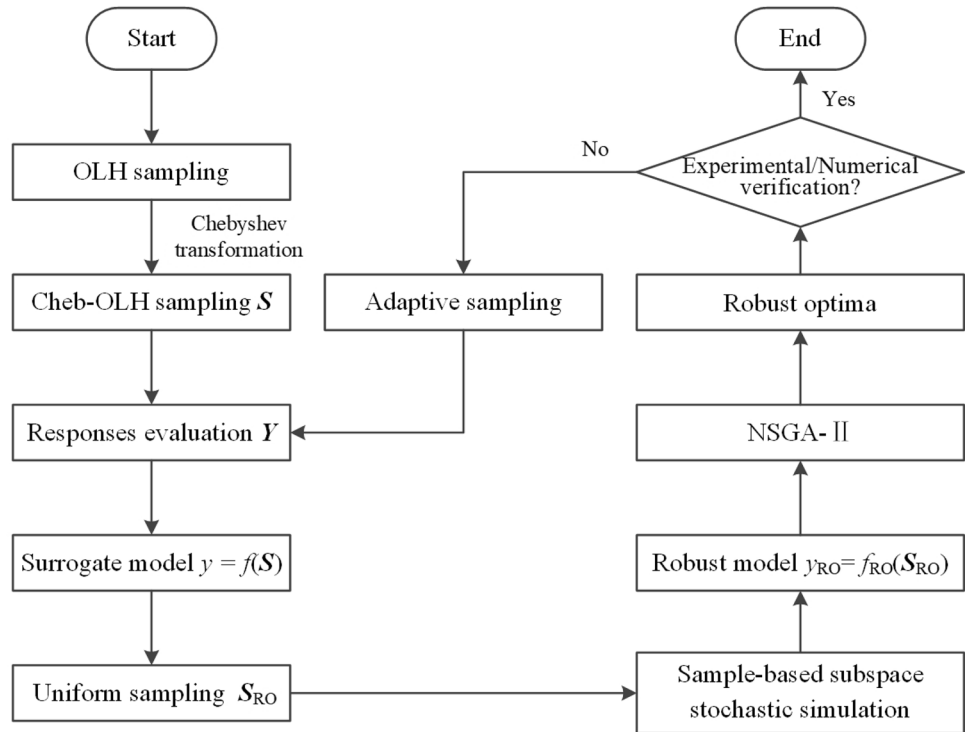
**Step 3:** *Construction of the outer robust model*

During this stage, the sample set is  $S_{RO}$  and the response is considered as  $\ln\sigma$ . And the outer robust model is established based on  $S_{RO}$  and  $\ln\sigma$ .

**Step 4:** *Global robust optimization*

The forecasting of response value is done with the inner Kriging model, while the outer robust model is utilized to predict the robustness indices. In the pursuit of multi-objective optimization, the Non-dominated Sorting Genetic Algorithm II (NSGA-II) (Deb et al. 2000)

**Fig. 3** Flowchart of robust optimization



is employed, resulting in the Pareto front. The NSGA-II algorithm boasts fast running speeds and excellent convergence of the solution set.

**Step 5: Determination and verification of global robust optimum**

In this step, both performance and robustness should be comprehensively considered. The global robust optimum should be selected from the Pareto front based on engineering practice. Ultimately, experimental or numerical techniques are utilized to validate the precision of the robust optimum. If the findings are trustworthy, the optimization process is finalized; if not, adaptive sampling, also known as sequential design, involves increasing the number of samples to enhance model accuracy.

**4 Benchmark tests**

Several benchmark mathematical problems are solved to illustrate the validity of the suggested design methodology. The test problems are selected from a variety of classical optimization test functions. Our current investigation focuses on design spaces with dimensions less than four, with plans for further study on higher dimensions based on the insights gained from our present results. For comparison, only the number of samples is varied, whereas the robust optimization process remains unchanged.

**4.1 One-dimensional function test**

A 10<sup>th</sup>-order polynomial is used to test the proposed robust optimization method, which is defined as follows:

$$\begin{aligned}
 f(x) = & 2.201370 \times 10^{-3}x^{10} - 1.052876 \times 10^{-1}x^9 + 2.151650x^8 \\
 & - 2.460697 \times 10^1x^7 + 1.734160 \times 10^2x^6 - 7.821379 \times 10^2x^5 \\
 & + 2.267874 \times 10^3x^4 - 4.114980 \times 10^3x^3 + 4.357030 \times 10^3x^2 \\
 & - 2.327900 \times 10^3x + 5.5 \times 10^2,
 \end{aligned}
 \tag{7}$$

where  $x \in [0, 10]$ . The four local optimal solutions of  $f(x)$  without considering robustness are shown in Table 1.

In considering robustness, it is important to note that the optimization results may change. We conducted tests using the proposed method to confirm this. Firstly, 29 samples were selected using Chebyshev extrema, and the real responses were calculated to build the Kriging model. Figure 4a displays the true function and Fig. 4b displays the inner Kriging model. Following this, an additional set of 100 samples was chosen uniformly across the design space

**Table 1** Local optimal solutions of  $f(x)$

No.	$x$	$f(x)$
1	0.620	73.313
2	2.836	92.231
3	7.402	321.378
4	9.695	20.651



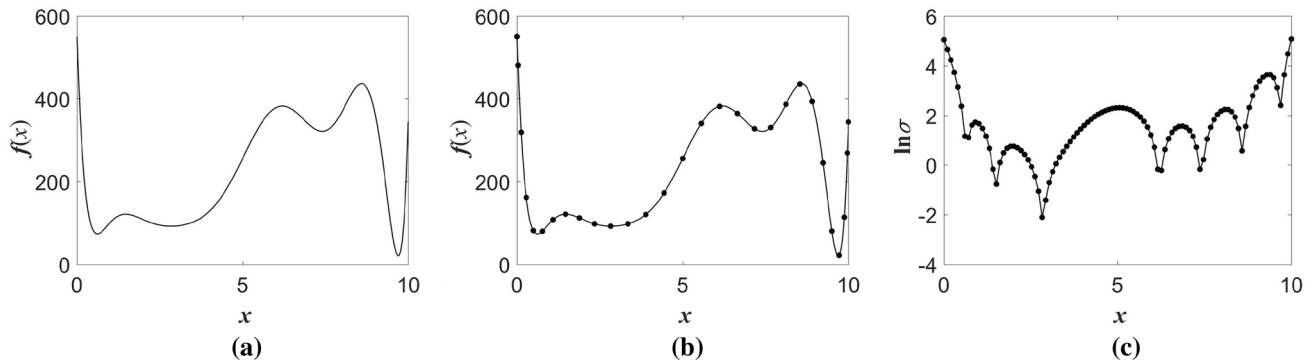


Fig. 4 One-dimensional function test. a Original function. b Inner Kriging model. c Outer robust model

and their standard deviations were calculated within a 5% neighborhood. Figure 4c shows the outer robust model.

In Fig. 4, the inner Kriging model and the original model exhibit remarkable alignment, showcasing four distinct local minimums. Conversely, the outer robust model displays a total of seven local minimums, which includes the previously mentioned four local minimums, as well as three local maximums.

The NSGA-II algorithm was employed for multi-objective optimization, the Pareto solutions are found to be concentrated mainly in three regions—the first, second, and fourth local optimal solutions in Table 1. This is because these positions represent both the locally optimal solutions of  $f(x)$  and  $\ln \sigma$ . The best solution with the smallest  $\ln \sigma$  is chosen, which offers the robust optimum as  $x = 2.0884$ ,  $f(x) = 105.1381$ , and  $\ln \sigma = -0.2913$ . The proposed method can achieve robust optimal results without getting stuck in local optima.

### 4.2 Two-dimensional function tests

To assess the effectiveness of the innovative sampling technique, we developed a Kriging model utilizing distinct sampling methods: OLH and Cheb-OLH. The Root Mean Square Error (RMSE) was employed for analyzing the overall accuracy of the Kriging model, which can be calculated using the following formula:

$$rmse = \sqrt{\sum_{i=1}^{m_t} (e^{(i)})^2 / m_t}, e^{(i)} = \|\hat{y}_t^{(i)} - y_t^{(i)}\|, \quad (8)$$

where  $m_t = m_0^n$  is the number of test samples,  $\hat{y}_t^{(i)}$  is the predicted value at test point  $i$ , and  $y_t^{(i)}$  is the true value at the same point.

The test was performed on a two-dimensional Rosenbrock function (Rosenbrock 1960) defined by

$$f(x_1, x_2) = 100(x_2 - x_1^2)^2 + (x_1 - 1)^2, \quad (9)$$

where  $x_1 \in [-2, 2], x_2 \in [-2, 2]$ . The function is unimodal, and the global minimum lies in a narrow, parabolic valley. The inner Kriging model is constructed with 29 OLH and Cheb-OLH samples, respectively. The RMSE of the former is 1.8959, while for the latter, it is notably smaller at 0.3906. To further demonstrate the ‘‘corner error’’ reduction by Cheb-OLH sampling, the error distribution of OLH and Cheb-OLH is presented in Fig. 5. The findings reveal that the maximal absolute error (AE) of OLH sampling occurred at the corner of the design space, and this was significantly reduced through the use of the Chebyshev transformation.

It is evident that the Kriging model created using the Cheb-OLH sampling method closely approximates the real function. Figure 6 shows the comparison of contours between the true function and the inner Kriging model. The robustness indices are determined using the inner Kriging model and the outer robust model is then constructed, as demonstrated in Fig. 7 by comparing predicted values to true values. The robust model contains several local optimal solutions situated in the gradual valley (Fig. 7a). To enhance the global accuracy of the multimodal function, the number of robust samples is set at intervals of  $10^2, 20^2, 30^2$ , and  $40^2$ . The global accuracy did not experience significant changes when the number of samples rose to  $30^2$ . Therefore, the number of robust model samples  $m_{RO} = 30^2$ , and the number of local subspace samples  $m_{SS} = 1600$ .

After conducting robust optimization, the results were chosen from the Pareto front, which is outlined in Table 2. Initially, robust optimum 1 was selected based on the smallest function value, without considering robustness. However, significant discrepancies between the predicted value and real value of  $\ln \sigma$  emerged. This can be attributed to the poor accuracy of the inner Kriging model near that point. The Cheb-OLH sampling prioritizes global

**Fig. 5** AE distribution of Rosenbrock function. **a** OLH. **b** Cheb-OLH

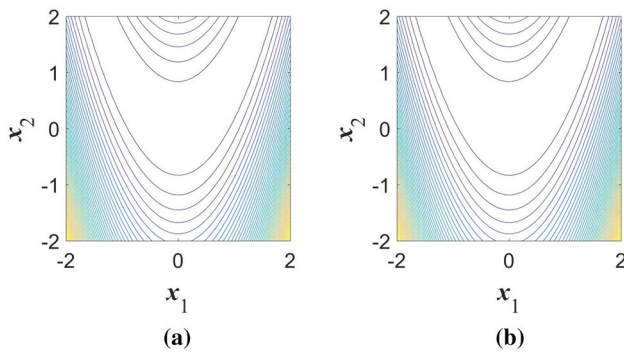
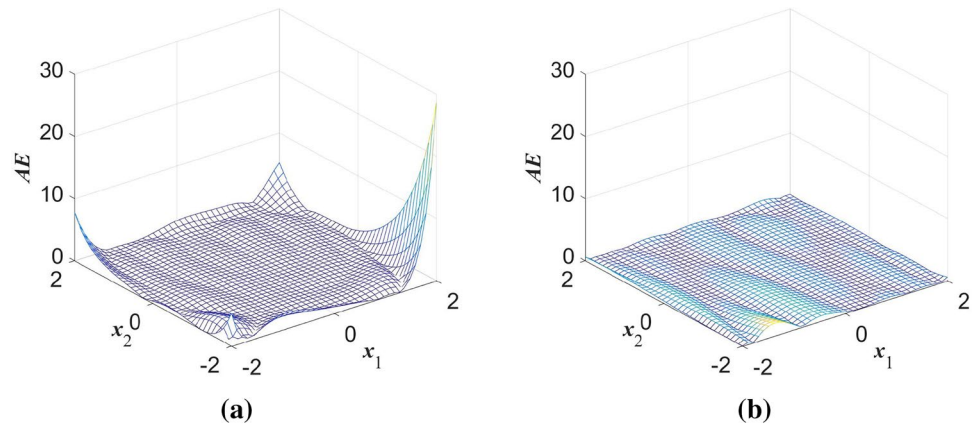


**Fig. 6** Contours of Rosenbrock function. **a** Original function. **b** Inner Kriging model

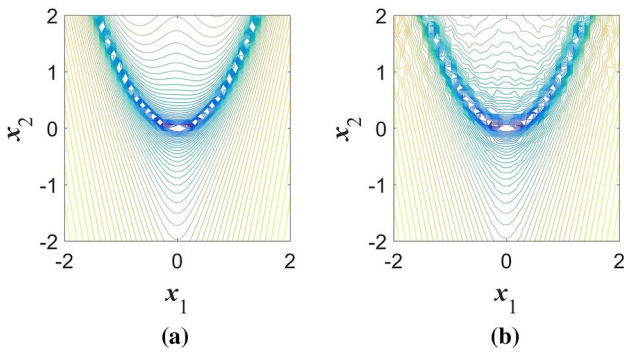


**Fig. 7** Contours of  $\ln\sigma$ . **a** True value. **b** Outer robust model

**Table 2** Robust optimization results of Rosenbrock function

	$(x_1, x_2)$	$f(x)$	$\ln\sigma$
Optimum	(1,1)	0	-0.78
Robust optimum 1	(1.24,1.55)	0.11	0.66
True value		0.06	-0.42
Robust optimum 2	(-0.21,0.06)	1.49	-1.83
True value		1.50	-1.99

accuracy, neglecting local accuracy near the optimal solution, which may account for this issue.

Based on the outer robust model, the best robust solution is robust optimum 2. This result is located near (0,0) and has a high level of robustness. Additionally, robust optimum 2 has good precision in both the predicted value and real value.

The Branin function (Branin 1972) is selected as another test function, which is defined by

$$f(x_1, x_2) = \left(x_2 - \frac{5.1}{4\pi^2}x_1^2 + \frac{5}{\pi}x_1 - 6\right)^2 + 10\left(1 - \frac{1}{8\pi}\right)\cos x_1 + 10 \tag{10}$$

where  $x_1 \in [-5, 5], x_2 \in [0, 15]$ . The upper bound of  $x_1$ , 10 is reduced to 5 to compare the two locally optimal solutions of  $f$ . Similar to the Rosenbrock function, the surrogate models are shown in Figs. 8 and 9, and the robust optimization results are shown in Table 3.

It can be seen from the table that the robust optimum 1 with the smallest function value still has a large error. While the robust optimum 2 with high level of robustness has higher precision. The result is similar to the Rosenbrock function due to large error near the global optimum. However, the global minimum and the robust optimum of the Branin function coincide. Despite these factors, we believe that robust optimum 2 is still a strong and reliable outcome for robust optimization.

### 4.3 Four-dimensional function tests

The first test was performed on a four-dimensional Trid function (Adorio and Diliman 2005), defined by

$$f(x) = \sum_{i=1}^n (x_i - 1)^2 - \sum_{i=2}^n x_i x_{i-1}, \tag{11}$$

**Fig. 8** Contours of Branin function. **a** Original function. **b** Inner Kriging model

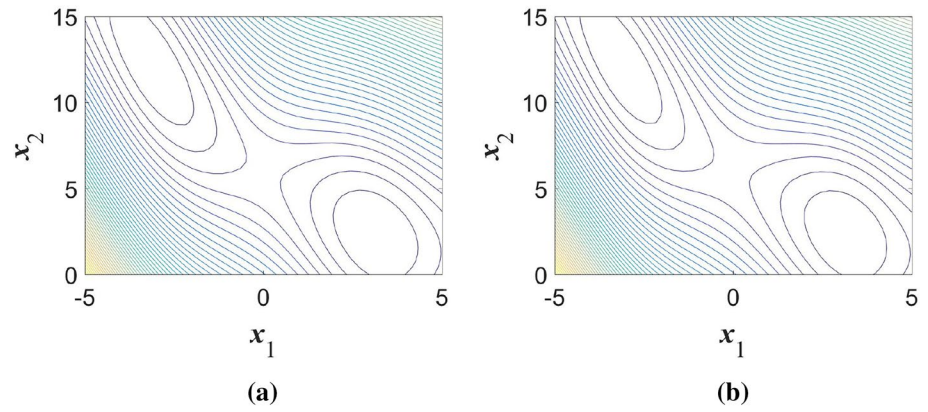


**Fig. 9** Contours of  $\ln\sigma$ . **a** True value. **b** Outer robust model

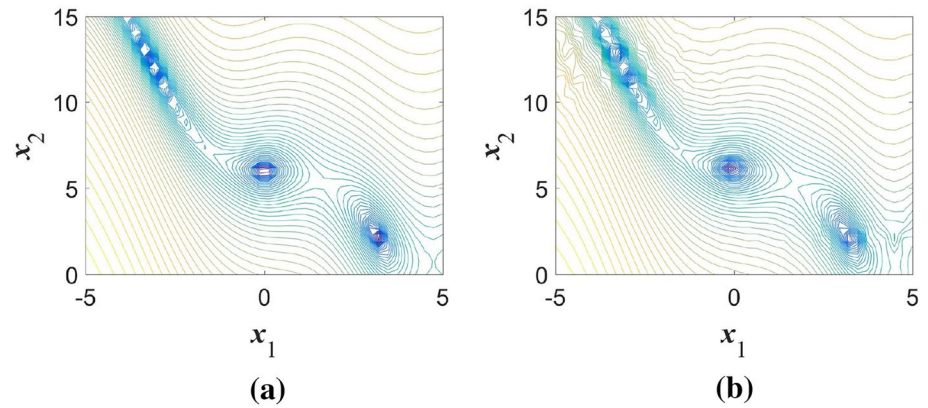


**Table 3** Robust optimization results of Branin function

	$(x_1, x_2)$	$f(x)$	$\ln\sigma$
Optimum 1	$(-\pi, 12.275)$	0.398	-2.69
Optimum 2	$(\pi, 2.275)$	0.398	-3.37
Robust optimum 1	$(3.17, 2.28)$	0.13	-2.46
True value		0.40	-3.19
Robust optimum 2	$(-0.10, 6.16)$	19.39	-2.89
True value		19.56	-2.78

**Table 4** Robust optimization results of Trid function

	$(x_1, x_2, x_3, x_4)$	$f(x)$	$\ln\sigma$
Optimum	$(4, 6, 6, 4)$	-16	-2.02
Robust optimum 1	$(3.99, 5.99, 5.92, 3.96)$	-15.99	0.63
True value		-15.99	-1.99
Robust optimum 2	$(0.19, 0.04, 0.01, 0.14)$	3.29	-0.20
True value		3.29	-0.24

where  $n$  is the dimensionality and  $n = 4$  in our study. The function is usually evaluated on the hypercube  $x_i \in [-n^2, n^2]$  for all  $i = 1, 2, \dots, n$ . For four-dimensional problems, the number of initial samples  $m = 137$ , the number of robust model samples  $m_{RO} = 5^4$ , and the number of local subspace samples  $m_{SS} = 1600$ . According to the robust optimization process proposed in Sect. 3, the results are shown in Table 4.

It is clear that the predicted value of the function is precise. This suggests that the inner Kriging model is also highly precise. However, it should be noted that  $\ln\sigma$  of robust optimum 1 is relatively large, which is the same as the result in the two-dimensional tests. This is because the Kriging has difficulty fitting multi-modal functions, especially when it comes to local optimal solutions.

The next test is the four-dimensional Styblinski-Tang function (Ustun et al. 2023) defined by

$$f(\mathbf{x}) = \frac{1}{2} \sum_{i=1}^n (x_i^4 - 16x_i^2 + 5x_i), \tag{12}$$

where  $n = 4$  and  $x_i \in [-5.12, 5.12], i = 1, 2, \dots, n$ . The robust optimization results of this function are shown in Table 5.

Although the inner Kriging model boasts high accuracy, the outer robust model predicts a significant deviation from the actual value. This could be attributed to two factors. Firstly, the number of robust samples may be insufficient, resulting in information loss during the construction of the multi-modal robust model. Secondly, the properties of the function may play a role. Unlike the Trid function, the



**Table 5** Robust optimization results of Styblinski-Tang function

	$(x_1, x_2, x_3, x_4)$	$f(x)$	$\ln\sigma$
Optimum	(- 2.90, - 2.90, - 2.90, - 2.90)	- 156.66	- 1.66
Robust optimum 1	(- 2.87, - 2.92, - 2.84, - 2.87)	- 160.10	1.04
True value		- 156.55	- 1.40
Robust optimum 2	(1.08, 1.12, 1.18, 1.15)	- 23.11	- 1.44
True value		- 26.45	0.49

Styblinski–Tang function has multiple local optima in the design space, which compromises the global accuracy of the inner Kriging model. This underscores the limitations of the Kriging when dealing with multi-modal functions.

Based on the above test results, the properties of the test function have a significant impact on the test results, particularly when there is more than one local optimal solution. Kriging is limited when dealing with multi-modal functions, and the error for the robustness indices is especially large at the minimum function value. However, for multiple test functions, the robust optimization method proposed in this paper can still achieve better robust design results.

On the other hand, the function of interest in practical engineering applications is sufficiently approximated by low-order polynomials (Soulat et al. 2013; Martins and Kennedy 2021) Therefore, the robust optimization based on Cheb-OLH sampling in this study can be useful for most engineering applications. Furthermore, for problems with multiple locally optimal solutions in function characteristics, localized sampling strategies can be employed when constructing the model, which is beyond the scope of this study.

### 5 Case study: Robust design optimization of RAE 2822 airfoil

During the manufacture of a wing, there are several uncertain factors that may result in deviations from the original design, thereby impacting its aerodynamic performance. Consequently, the design of airfoil aerodynamic performance is regarded as a quintessential robust design problem. In this study, the aerodynamic robust optimization of the RAE 2822 airfoil is carried out to verify the proposed method. Moreover, the geometric parameters of RAE 2822 airfoil are chosen as the design variables.

#### 5.1 Airfoil profile parameterization

There are two primary methods for parameterizing airfoils, namely deformative and constructive methods. Deformative methods involve modifying an existing airfoil to create

a new shape. Conversely, constructive methods define the new airfoil shape based solely on the design variables. Notable examples of deformative methods include Hicks–Henne Bump Functions (Nemati and Jahangirian 2020) and Radial Basis Function Domain Element (Rendall and Allen 2008), while constructive methods encompass Class Function/Shape Function Transformations (CST) (Kulfan 2007), B-Splines, and PARSEC (Sobieczky 1999).

The Hicks–Henne function can obtain a smooth geometric shape and has the advantage of high accuracy and stability. It generates subtle perturbations based on the reference airfoil without nonphysical geometry, thus it is applicable and selected for airfoil profile parameterization in the manufacturing error uncertainty analysis. The expressions of the Hicks–Henne function are described as follows:

$$y_{up}(x) = y_{0up}(x) + \sum_{k=1}^{n_p/2} P_k f_k(x) \quad , \quad (13)$$

$$y_{low}(x) = y_{0low}(x) + \sum_{k=n_p/2+1}^{n_p} P_k f_k(x) \quad , \quad (14)$$

where  $y_{up}$  and  $y_{low}$  represent the upper and lower surface functions of the airfoil, respectively.  $y_{0up}$  and  $y_{0low}$  represent the upper and lower surface functions of the base airfoil, respectively.  $x$  represents the chord length of the airfoil, which ranges from 0 to 1.  $n_p$  is the number of type functions, determined according to the design requirements.  $k$  is the number of variables controlling key points of airfoil thickness distribution.  $P_k$  is a design variable, and the airfoil shape is changed by assigning a value to  $P_k$ .  $f_k(x)$  is the Hicks–Henne basis function, which is defined as follows:

$$f_k(x) = \begin{cases} x^{0.25}(1-x)e^{-20x}, & k = 1 \\ \sin^3(\pi x^{e(k)}), & 2 \leq k \leq n_p - 1 \end{cases} \quad , \quad (15)$$

$$e(k) = \frac{\log 0.5}{\log x_k}, 0 < x_k < 1 \quad , \quad (16)$$

where  $x_k$  is the node chosen between the leading and trailing edge of the airfoil.

Due to the geometric error near the leading edge has a more important influence on the airfoil (Zhao et al. 2017), four parameters  $P_1, P_2, P_3, P_4$  are selected as the uncertain variables. In this study, the airfoil non-dimensional chord length is set to 1,  $x_1$  is 0, and  $x_2$  is 0.03. The corresponding ranges of Hicks–Henne function coefficients  $P_1, P_2, P_3$  and  $P_4$  are  $[-0.005, 0.005]$ . With such level of geometric uncertainty, the samples with leading edge uncertainties for airfoil RAE2822 are shown in Fig. 10.

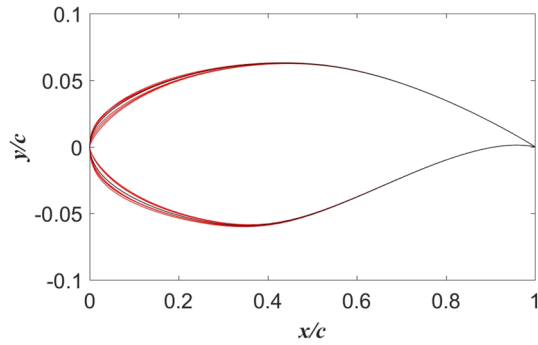


Fig. 10 Samples with leading edge uncertainties for airfoil RAE 2822

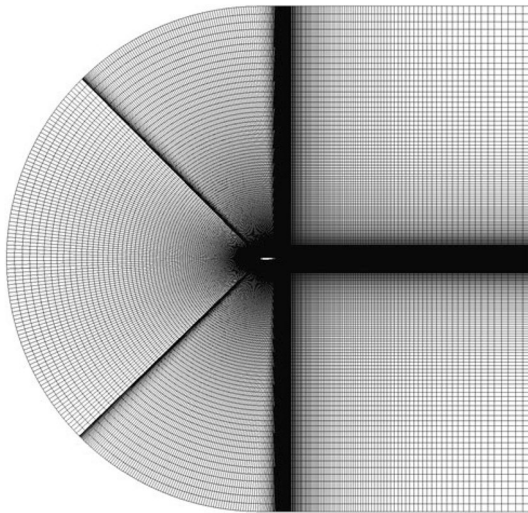


Fig. 11 Calculation domain and mesh for RAE 2822

### 5.2 Numerical simulation and validation

The RAE 2822 transonic airfoil simulation is solved by steady-state Reynolds-Averaged Navier–Stokes (RANS) equations together with a SST  $k - \omega$  turbulence model closure. The nominal flow conditions are the ones described in Cook et al. (1979) for the test case #13A. The nominal free-stream Mach number  $M = 0.74$ , angle of attack  $\alpha = 3.19^\circ$ , and Reynolds number  $Re = 2.7 \times 10^6$ . Since the wind tunnel experiment is disturbed by the wind tunnel wall at the same angle, the angle of attack needs to be corrected for the numerical calculation condition of free incoming flow (Lin 2021). According to existing study (Coakley 1987), the angle of attack is revised to  $2.8^\circ$ , and the Mach number remains unchanged.

The calculation domain for RAE 2822 is two-dimensional C-type topology, as shown in Fig. 11. The length and width of which are 30 times chord length, and the airfoil surface is modeled as a no-slip wall. To ensure accuracy, the first layer of the grid near the wall has a height of  $10^{-5}$  times the chord

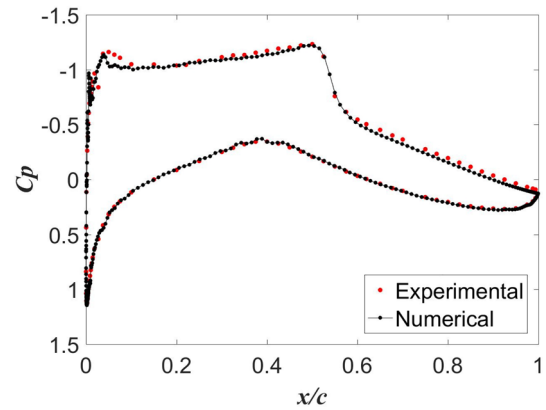


Fig. 12 Comparison of pressure coefficient distribution

Table 6 Comparison of experiment and CFD

	$C_l$	$C_d$
Experiment	0.733	0.0188
CFD	0.70745	0.02017
Relative error	-3.49%	7.29%

length, and the local fine mesh is applied to keep  $y^+$  below 1. The pressure algorithm and the second-order upwind difference scheme are applied, with the convergence criterion of residual less than  $1 \times 10^{-5}$ .

To validate the numerical simulation method, the lift coefficient ( $C_l$ ) and drag coefficient ( $C_d$ ) acquired through CFD simulation were compared with experimental results (Cook et al. 1979), as presented in Table 6. Additionally, the pressure coefficient ( $C_p$ ) of the airfoil surface was also compared, as shown in Fig. 12. The results reveal that the margin of error for both drag and lift coefficients is lower than 10%, while the curve of the pressure coefficient displays remarkable consistency. Therefore, the CFD simulation has effectively validated the performance prediction of the RAE 2822 airfoil.

### 5.3 Optimization of aerodynamic performance and robustness indices

Global robust optimization is performed to enhance the performance and the robustness of RAE 2822 airfoil, which can be formulated as

$$\text{minimize} \begin{cases} C_d \\ -C_l \\ \ln \sigma(C_d) \\ \ln \sigma(C_l) \end{cases}, \quad (17)$$

subject to  $P_k \in [-0.005, 0.005]$

where  $P_k$  are design variables for  $k = 1, 2, 3$  and 4.

A total of 137 samples were generated using OLH and transformed based on the positions of the Chebyshev extrema, as proposed in Sect. 2. These samples formed 137 different parametric geometric models. CFD simulations were performed on each of these models, and the values of  $C_d$  and  $C_l$  were obtained. Based on the data, the inner Kriging surrogate model was constructed for the two objectives.

Next, the number of robust model samples  $m_{RO}$  was set to  $5^4$  and the number of local subspace samples  $m_{SS}$  was set to 1600. The robustness indices were calculated based on the inner Kriging model and the outer robust model was constructed.

Surrogate-based multi-objective optimization was performed by adopting the NSGA-II algorithm with an initial population of 2000, evaluated over 30 generations.

Regardless of the robustness of the design, the goal is to minimize  $C_d$  and maximize  $C_l$ . The Pareto front is shown in Fig. 13a. The optimal solution was chosen based on the lift-drag ratio and marked as opt1.

Then, the objectives  $\ln\sigma(C_d)$  and  $\ln\sigma(C_l)$  were selected for the two-objective optimization process (Fig. 13b). Consequently, the lift-drag ratio was still taken into consideration under the premise of enhancing robustness. And the robust optimal solution was selected and denoted as opt2.

Finally, a comprehensive 4-objective optimization was executed. Two optimal solutions were selected from the Pareto solutions. Opt3 signifies a scenario where the performance is maximized without sacrificing robustness, while opt4 represents the optimal solution for maintaining robustness while achieving the desired performance level. The results of the four optimizations are depicted in Fig. 13.

From Fig. 13, it is clear that while traditional optimal design (opt1) can achieve optimal airfoil performance, the robustness of its lift coefficient is significantly reduced. This means that any manufacturing errors on the airfoil surface

may impact its performance, and the desired design result may not be achieved. On the other hand, optimizing only the robustness indices (opt2) can enhance the robustness of the airfoil and reduce the impact of uncertain factors on its performance. However, the performance of the airfoil will be decreased. Hence, there are some defects in the above two design results.

The results of four-objective optimization (opt3 and opt4) are close to the Pareto solutions in terms of performance and have improved robustness compared to the initial design. Nevertheless, obtaining minimum values for both aerodynamic performances and robustness indices concurrently is unattainable. Consequently, choosing the optimal solution necessitates weighing trade-offs and making compromises.

The robust optimization results are compared with the reference configuration in Table 7. Opt3 managed to increase  $C_l$  by 1.94% compared to the reference configuration and decrease  $C_d$  by 2.53%. Opt4 managed to increase  $C_l$  by 2.19% compared to the reference configuration and decrease  $C_d$  by 2.08%. At the same time, its robustness indices are also improved, which fully reflects the superiority of this robust design method.

In the benchmark test, the insufficient accuracy of the model results in inaccurate calculation of the robustness indices. Therefore, CFD simulation and verification of optimization results are required. The predictions differed slightly from the CFD results (Table 7). The differences were not greater than 1% for the four optimal results, which were within the numerical uncertainty of the CFD simulations.

The geometric profile comparison between the airfoil of opt3, opt4, and the reference airfoil is presented in Fig. 14. It can be observed that the lower surface of opt3 closely aligns with the reference airfoil, while its upper surface exhibits an enlargement in the Y-direction. These results suggest that a larger leading edge profile tends to enhance performance

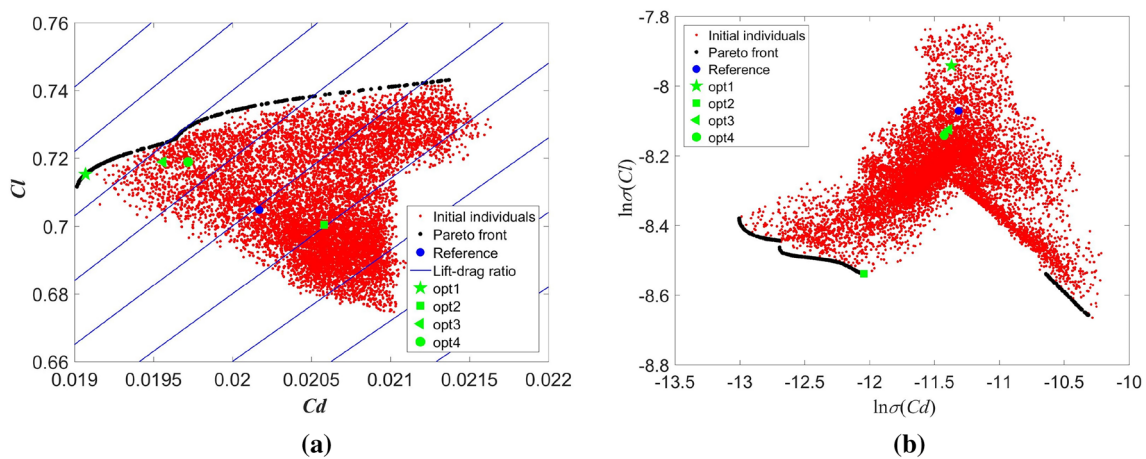


Fig. 13 Pareto front. a Aerodynamic performance. b Robustness indices

and reduce sensitivity to uncertainties. Despite a reduction in size on the lower surface of opt4 airfoil, its performance and robustness are still improved due to the expansion of its upper surface. This highlights that the upper surface plays a predominant role in determining the overall aerodynamic characteristics of an airfoil.

Figure 15a reveals a higher peak of suction closer to the leading edge in the optimized airfoil, indicating an increase in suction on the upper surface and an improvement in the lift coefficient. The leading edge robust optimization also induces a slight negative displacement of the shock position along the  $X$ -axis, as illustrated in Fig. 15b.

**Table 7** Results of multi-objective robust optimization

	$P_k(\times 10^{-3})$	$C_d$	$C_l$	$\ln\sigma(C_d)$	$\ln\sigma(C_l)$
Reference	(0, 0, 0, 0)	0.02017	0.70745	-11.31	-8.07
Opt1	(4.99, 0.74, -4.94, -3.20)	0.01907	0.71528	-11.37	-7.94
Opt1 CFD		0.01928	0.71616		
Opt2	(0.09, -2.50, 1.47, 4.72)	0.02058	0.70036	-12.04	-8.54
Opt2 CFD		0.02061	0.70067		
Opt3	(4.19, 0.82, -2.09, 0.71)	0.01956	0.71891	-11.39	-8.12
Opt3 CFD		0.01966	0.71850		
Opt4	(3.86, 0.87, -0.11, 2.50)	0.01972	0.72026	-11.43	-8.14
Opt4 CFD		0.01975	0.72016		

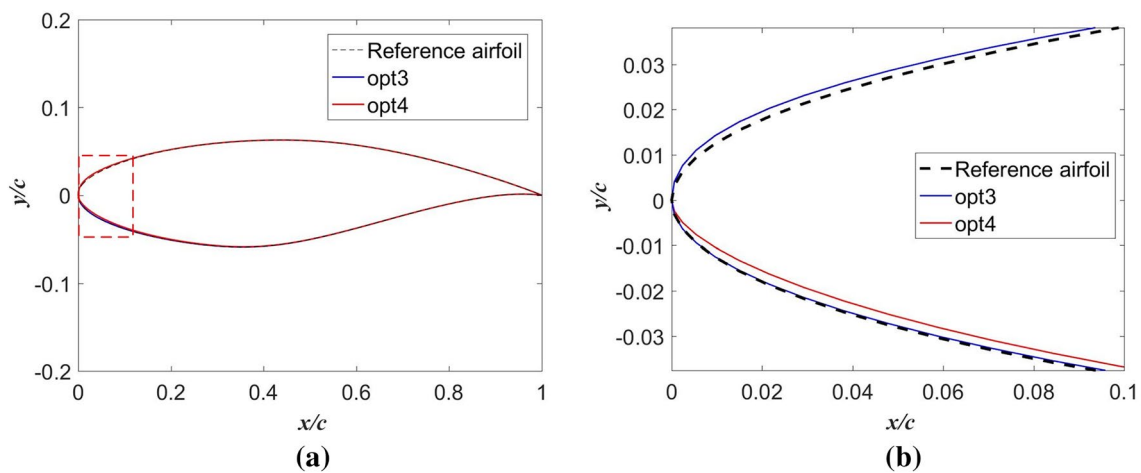
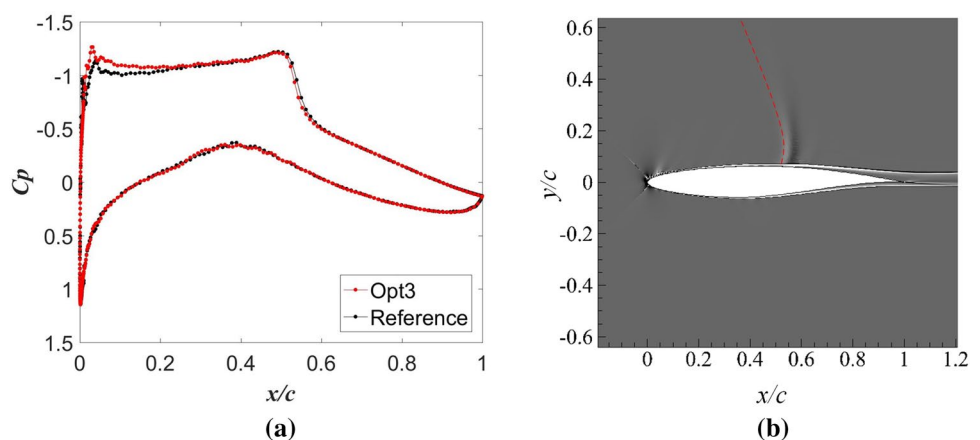


**Fig. 14** Comparisons of airfoil profiles. **a** Whole profile. **b** Profile zoomed to the leading edge

**Fig. 15** Comparison of opt3 and reference airfoil. **a** Pressure coefficient distribution. **b** Shadowgraph





Normally, fluid flows in a pro-pressure direction, from high-pressure to low-pressure areas. However, an anomalous flow direction is observed starting from the peak of the upper airfoil, where the fluid moves from the low-pressure to high-pressure area. This phenomenon is referred to as an inverse pressure gradient, which leads to the conversion of kinetic energy of the upper airflow into pressure potential energy along the  $X$ -direction. The robust optimization of the airfoil involves passivation of the leading edge and a slight reduction in the length of the inverse pressure gradient region along the  $X$ -direction. Nevertheless, there is higher boundary layer energy and increased lift force generated by the suction surface compared to reference conditions.

To better understand the functional mapping from the design space to the objective space, the Self-Organizing Map (SOM) (Kohonen 1990) visualization was created with all initial individuals and optimization results, as shown in Fig. 16. The SOM is a type of neural network designed to understand high-dimensional data using low-dimensional representations. Each variable is depicted as a two-dimensional map which preserves the topological properties of the initial individuals. One individual is always found at the same two-dimensional position from one map to another and distinguished from the other individuals according to their colors, which represent the magnitude of the variable.

In Fig. 16, the eight maps represent the values of the four variables and the four objectives. The positive correlation is obviously observed between  $P_2$  and  $C_l$ . In the local region, there is a certain correlation between  $P_1$  and  $C_l$ . However, there is an absence of any meaningful association between  $P_3, P_4$  and  $C_d, C_l$ . This suggests that the lift coefficient of RAE 2822 airfoil is more closely linked to its upper surface shape. Furthermore, there is no correlation between  $C_d, C_l$  and their standard deviations.

## 6 Conclusion

In this study, a Chebyshev-transformed OLH sampling method is proposed to perform a robust aerodynamic design optimization. The method was inspired by the functional potential theory which can solve the ‘‘Runge effect’’ problem, and the Chebyshev transformation was extended to higher-dimensional design space, thus improving the global accuracy of the surrogate model and reducing the corner error. A novel robust optimization technique has been introduced based on the surrogate model. The method involves computing robustness indices and constructing a robustness model via a high-precision surrogate model. Through the application of robust optimization and utilizing both models, the robust design optimization results can be enhanced without sacrificing performance.

Theoretical tests were performed on a variety of benchmark functions ranging from one-dimensional to four-dimensional cases. All the tests favored the proposed method. However, in the process of testing, there is also a problem of insufficient local sampling points. For this problem, locally intensive methods should be applied.

Based on the Cheb-OLH sampling and surrogate model, a multi-objective robust optimization succeeded in boosting the aerodynamic performance and robustness of the RAE 2822 airfoil. Compared with the reference, the optimized design improved the lift coefficient by 1.94% and drag coefficient by 2.53%. Moreover, the robustness indices also improved by nearly 1%. For all robust optimal results, the differences between the predictions of the surrogate model and the CFD simulation results were less than 1%. The reduction in corner error using the Cheb-OLH sampling method and the robust design based on surrogate model are favorable, which is worthy of further promotion for many other engineering applications.

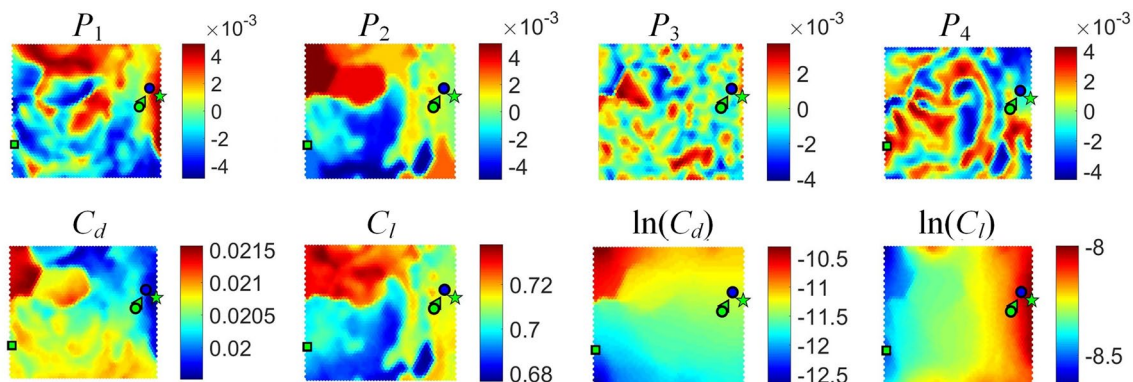


**Fig. 16** SOM visualization of dominated points, reference (blue point), opt1 (green pentacle point), opt2 (green square point), opt3 (green triangle point), and opt4 (green circle point). (Color figure online)

**Acknowledgments** This research was supported by the National Natural Science Foundation of China (Grant Nos. 12272354 and 12302229), the Natural Science Foundation of Henan Province (Grant No. 222300420547), and Postdoctoral Fellowship Program of China Postdoctoral Science Foundation (Grant No. GZC20232400). This work was supported by the National Supercomputing Center in Zhengzhou, as well as Hefei Advanced Computing Center. The authors acknowledge HEXAGON MSC CRADLE for the CFD solver licenses provided.

**Author contributions** Corresponding author Zebin Zhang: (zebin.zhang@zzu.edu.cn) and Author Xianzong Meng: (xianzongmeng@zzu.edu.cn) are co-corresponding authors of this paper.

## Declarations

**Conflict of interest** The authors have no conflict of interest to declare that are relevant to the content of this article.

**Replication of results** The detailed process of the proposed Cheb-OLH sampling and the surrogate-based robust design optimization are shown in Sects. 2 and 3. Codes and datasets for replication can be provided upon request from the corresponding author.

## References

- Adorio, EP, Diliman UP (2005) MVF-multivariate test functions library in C for unconstrained global optimization
- Beyer HG, Sendhoff B (2007) Robust optimization—a comprehensive survey. *Comput Methods Appl Mech Eng* 196(33–34):3190–3218
- Branin FH (1972) Widely convergent method for finding multiple solutions of simultaneous nonlinear equations. *IBM J Res Dev* 16(5):504–522
- Cioppa T, Lucas TW (2007) Efficient nearly orthogonal and space-filling latin hypercubes. *Technometrics* 49(1):45–55
- Coakley T (1987) Numerical simulation of viscous transonic airfoil flows. In: AIAA 25th Aerospace Sciences Meeting
- Cook PH, McDonald MA, Firmin MCP (1979) AGARD advisory report No. 138 experimental data base for computer program assessment
- Deb K, Agrawal S, Pratap A, Meyarivan T (2000) A fast elitist non-dominated sorting genetic algorithm for multi-objective optimization: NSGA-II. *Lect Notes Comput Sci* 1917(5):849–858
- Dong B, Lu Z (2022) Efficient adaptive kriging for system reliability analysis with multiple failure modes under random and interval hybrid uncertainty. *Chin J Aeronaut* 35(5):333–346
- Driscoll TA, Hale N, Trefethen LN (2014) Editors, *chebfun guide*, pafnuty publications
- Fang K (1994) *Uniform design and uniform design table*. Science Press, Beijing
- Fang H, Gong C, Li C, Zhang Y, Ronch AD (2021) A sequential optimization framework for simultaneous design variables optimization and probability uncertainty allocation. *Struct Multidisc Optim* 63(3):1307–1325
- Fu C, Zhu W, Yang Y, Zhao S, Lu K (2022) Surrogate modeling for dynamic analysis of an uncertain notched rotor system and roles of chebyshev parameters. *J Sound Vib* 524:116755
- Giunta A, Wojtkiewicz S, Eldred M (2003) Overview of modern design of experiments methods for computational simulations. In: 41st Aerospace Sciences Meeting and Exhibit
- Hanazaki K, Yamazaki W (2024) Robust design optimization of supersonic biplane airfoil using efficient uncertainty analysis method for discontinuous problem. *Aerospace* 11(1):64
- Iuliano E (2019) Efficient design optimization assisted by sequential surrogate models. *Int J Aerosp Eng* 1:1–34
- Jaeger L, Gogu C, Segonds S, Bes C (2013) Aircraft multidisciplinary design optimization under both model and design variables uncertainty. *J Aircr* 50(2):528–538
- Jiang C, Zheng J, Han X (2018) Probability-interval hybrid uncertainty analysis for structures with both aleatory and epistemic uncertainties: a review. *Struct Multidisc Optim* 57(6):2485–2502
- Jones DR, Martins JRRR (2021) The direct algorithm: 25 years later. *J Global Optim* 79(3):521–566
- Kohonen T (1990) The self-organizing map. *Proc IEEE* 78(9):1464–1480
- Kulfan B (2007) A universal parametric geometry representation method - CST. In: 45th AIAA Aerospace Sciences Meeting and Exhibit
- Leary S, Bhaskar A, Keane A (2003) Optimal orthogonal-array-based latin hypercubes. *J Appl Stat* 30(5):585–598
- Lee SW, Kwon OJ (2006) Robust airfoil shape optimization using design for six sigma. *J Aircr* 43(3):843–846
- Lee KH, Park GJ (2006) A global robust optimization using kriging based approximation model. *JSME Int J Ser C* 49(3):779–788
- Lin ZF (2021) Research on efficient global aerodynamic optimization design algorithm based on co-kriging model. PhD thesis, National University of Defense Technology
- Martins JRRR, Kennedy GJ (2021) Enabling large-scale multidisciplinary design optimization through adjoint sensitivity analysis. *Struct Multidisc Optim* 64(5):2959–2974
- Nemati M, Jahangirian A (2020) Robust aerodynamic morphing shape optimization for high-lift missions. *Aerosp Sci Technol* 103:105897
- Pang Y, Lai X, Zhang S, Wang Y, Yang L, Song X (2023) A Kriging-assisted global reliability-based design optimization algorithm with a reliability-constrained expected improvement. *Appl Math Model* 121:611–630
- Plaskota L, Wasilkowski GW (2004) Smolyak's algorithm for integration and  $l_1$ -approximation of multivariate functions with bounded mixed derivatives of second order. *Numer Algorithms* 36(3):229–246
- Rendall TCS, Allen CB (2008) Unified fluid-structure interpolation and mesh motion using radial basis functions. *Int J Numer Meth Eng* 74(10):1519–1559
- Ribaud M, Blanchet-Scalliet C, Helbert C, Gillot F (2020) Robust optimization: a kriging-based multi-objective optimization approach. *Reliab Eng Syst Saf* 200:106913
- Rosenbrock HH (1960) A automatic method for finding the greatest or least value of a function. *Comput J* 3(3):174–184
- Sobieczky H (1999) Parametric airfoils and wings. *Recent Dev Aerodyn Des Methodol* 65:71–87
- Song C, Yang X, Song W (2018) Multi-infill strategy for kriging models used in variable fidelity optimization. *Chin J Aeronaut* 31(3):448–456
- Soulat L, Ferrand P, Moreau S, Aubert S, Buisson M (2013) Efficient optimisation procedure for design problems in fluid mechanics. *Comput Fluids* 82:73–86
- Tang T, Zhou T (2015) Recent developments in high order numerical methods for uncertainty quantification. *Sci Sinica* 58(7):891
- Tao J, Sun G (2019) Application of deep learning based multi-fidelity surrogate model to robust aerodynamic design optimization. *Aerosp Sci Technol* 92:722–737
- Trefethen LN (2013) *Approximation theory and approximation practice*. Society for Industrial and Applied Mathematics (SIAM), Philadelphia, PA
- Ullrich T (2008) Smolyak's algorithm, sampling on sparse grids and sobolev spaces of dominating mixed smoothness. *East J Approx* 14(1):1–38

- Ustun D, Erkan U, Toktasand A, Lai Q, Yang L (2023) 2D hyperchaotic Styblinski–Tang map for image encryption and its hardware implementation. *Multimed Tools Appl* 83(12):34759
- Wang P, Bai Y, Lin C, Han X (2024) A hybrid criterion-based sample infilling strategy for surrogate-assisted multi-objective optimization. *Struct Multidisc Optim* 67(3):44
- Wu J, Luo Z, Zhang N, Zhang Y (2015) A new interval uncertain optimization method for structures using chebyshev surrogate models. *Comput Struct* 146:185–196
- Wu X, Zhang W, Song S (2018) Robust aerodynamic shape design based on an adaptive stochastic optimization framework. *Struct Multidisc Optim* 57(2):639–651
- Zhang Z, Demory B, Henner M, Ferrand P, Gillot F, Beddadi Y, Franquelin F, Marion V (2014) Space infill study of kriging meta-model for multi-objective optimization of an engine cooling fan. In: *ASME Turbo Expo 2014: Turbine Technical Conference and Exposition*
- Zhang Z, Han Z, Ferrand P (2019) High anisotropy space exploration with co-kriging method. In: *Proceedings Lego - 14th International Global Optimization Workshop*
- Zhang Z, Jing S, Li Y, Meng X (2024) Corner error reduction by chebyshev transformed orthogonal grid, in press. *Engineering with Computers*
- Zhao K (2015) Complex aerodynamic optimization and robust design method based on computational fluid dynamics. PhD thesis, Northwestern Polytechnical University
- Zhao H, Gao Y, Wang C (2017) Effective robust design of high lift nlf airfoil under multi-parameter uncertainty. *Aerosp Sci Technol* 68:530–542
- Zhao H, Gao Z, Xu F, Zhang Y (2019) Review of robust aerodynamic design optimization for air vehicles. *Arch Comput Methods Eng* 26(3):685–732

**Publisher's Note** Springer Nature remains neutral with regard to jurisdictional claims in published maps and institutional affiliations.

Springer Nature or its licensor (e.g. a society or other partner) holds exclusive rights to this article under a publishing agreement with the author(s) or other rightsholder(s); author self-archiving of the accepted manuscript version of this article is solely governed by the terms of such publishing agreement and applicable law.